UC Riverside

UC Riverside Previously Published Works

Title

Planar laser induced fluorescence for temperature measurement of optical thermocavitation

Permalink

https://escholarship.org/uc/item/74v2g5p9

Authors

Banks, D
Robles, V
Zhang, B
et al.

Publication Date

2019-05-01

DOI

10.1016/j.expthermflusci.2019.01.030

Peer reviewed

eScholarship.org Powered by the California Digital Library
University of California

Experimental Thermal and Fluid Science 103 (2019) 385–393

Contents lists available at ScienceDirect

Experimental Thermal and Fluid Science

journal homepage: www.elsevier.com/locate/etfs

Planar laser induced fluorescence for temperature measurement of optical thermocavitation

D. Banks[a,b], V. Robles[b], B. Zhang[b,c], L.F. Devia-Cruz[b], S. Camacho-Lopez[d], G. Aguilar[b,*]

[a] Department of Mechanical Engineering, California State University Fullerton, Fullerton, CA 92831, USA
[b] Department of Mechanical Engineering, University of California, Riverside, Riverside 92521, CA, USA
[c] School of Energy and Power Engineering, Xi'an Jiaotong University, Xi'an 710049, PR China
[d] Centro de Investigación Científica y de Educación Superior de Ensenada, Departamento de Óptica, Carretera Ensenada – Tijuana 3918, Zona Playitas, Ensenada, B.C. C. P. 22860, Mexico

ARTICLE INFO

Keywords:
Shadowgraph imaging
Laser-induced cavitation
Acoustic dissipation

ABSTRACT

Pulsed laser-induced cavitation, has been the subject of many studies describing bubble growth, collapse and ensuing shock waves. To a lesser extent, hydrodynamics of continuous wave (CW) cavitation or thermocavitation have also been reported. However, the temperature field around these bubbles has not been measured, partly because a sensor placed in the fluid would interfere with the bubble dynamics, but also because the short-lived bubble lifetimes (~70–200 μs) demand high sampling rates which are costly to achieve via infrared (IR) imaging. Planar laser-induced fluorescence (PLIF) provides a non-intrusive alternative technique to costly IR imaging to measure the temperature around laser-induced cavitation bubbles.

A 440 nm laser sheet excites rhodamine-B dye to fluoresce while thermocavitation is induced by a CW 810 nm laser. Post-calibration, the fluorescence intensity captured with a high-speed Phantom Miro camera is correlated to temperature field adjacent to the bubble. Using shadowgraphy and PLIF, a significant decrease in sensible heat is observed in the nucleation site– temperature decreases after bubble collapse and the initial heated volume of liquid shrinks. Based on irradiation time and temperature, the provided optical energy is estimated to be converted up to 50% into acoustic energy based on the bubble's size, with larger bubbles converting larger percentages.

1. Introduction

Research in cavitation dynamics for preventing undesired damage has been largely oversaturated, specifically studies of cavitation induced by pulsed lasers. This work focuses on cavitation bubbles induced by continuous wave (CW) lasers for the purposes of heat management. Optical cavitation was first observed when a ruby pulsed laser was focused into water by Carome et al. [1]. Since then, cavitation has been induced by pulsed and continuous wave lasers [2,3] and has seen applications in biomedicine [4], microfluidics [5], fluid composition studies [6], and nanoscale engineering [7], among others. Pulsed laser cavitation tends to be more commonly reported; the energy density of short-duration laser pulses often exceeds that of continuous lasers and can ionize the target liquid, readily nucleating a bubble [8]. Yavas, using at krypton fluoride pulsed laser, estimated nucleation temperatures of 150 °C in water while exploring the minimum fluences required to induce cavitation [9]. CW laser cavitation, typically with a lower energy density compared to pulsed lasers, has not been seen to ionize the liquid. Instead, in a relatively much slower process, the laser beam superheats the irradiated volume to vaporization, as reported by Padilla-Martinez et al, based on simulations [10]. CW-induced cavitation can therefore be referred to as 'thermocavitation'. Experimentally, Quinto-Su et al. [11], found that for pulsed laser cavitation, only a small and short-lived heating effect occurred (13 °C, 1 ms), in contrast to the extended heating period expected for the CW-induced process. However, experimental studies of the heating processes associated with CW cavitation have not been reported.

In the context of thermocavitation, the heating process is extended and expanded significantly over the near-instantaneous dynamics of pulsed laser-induced cavitation. The optical energy absorbed by the liquid plays a major role as it heats the liquid locally and relatively slowly—compared to pulsed lasers, prior to cavitation. During this process, the refractive index of the working liquid is changed within the heated volume. In comparison, pulsed lasers induce a phase change on

* Corresponding author.
E-mail address: gaguilar@engr.ucr.edu (G. Aguilar).

https://doi.org/10.1016/j.expthermflusci.2019.01.030
Received 23 August 2018; Received in revised form 8 January 2019; Accepted 26 January 2019
Available online 28 January 2019
0894-1777/ © 2019 Elsevier Inc. All rights reserved.

the leading edge of the pulse, avoiding the comparatively slow heating around the laser focal volume seen in CW cavitation. Thermocavitation could be used to produce micrometric local liquid flow non-intrusively at targeted locations, particularly in microfluidic devices such as lab-on-a-chip systems [12], where due to the small length scales, turbulent mixing is challenging to create. In these systems, the rapid growth and collapse of micrometric bubbles formed near the heat transfer area, could actively agitate the surrounding liquid and thus enhance convective heat transfer. During bubble formation and expansion, fluid is expected to be displaced away from the active surface of heat exchange, thus enhancing convection. However, it is during bubble collapse where a more significant mixing and cooling is expected. Since thermocavitation bubbles form at the liquid interface, an asymmetry known as microstreaming forms a jet that pulls the bubble pole towards the nearest solid boundary, drawing liquid toward the surface. This dynamic feature has been exploited using acoustically vibrated bubbles in micro-scale mixing applications, facilitating fast homogeneous mixing in otherwise unmixed reservoirs [13]. Based on these principles, optical cavitation can enhance convective cooling by pulling cold liquid from an unheated bulk fluid towards a hot boundary.

Using thermocavitation as a cooling aid appears unreasonable because it is a heating process – the focal volume is heated to near its spinodal limit [6]. Without an additional process to disperse the added heat, any additional convective cooling would be negated. The fate of the energy used to produce cavitation determines the cavitation effectiveness as a cooling mechanism. Two approaches may reduce the heat necessary to produce cavitation. First, facilitation of low-energy cavitation can be accomplished using liquids that nucleate at lower boiling temperatures and/or with low latent heat. One example of this approach is the work of Rastopov and Sukhodolsky, who found that the optical energy required for cavitation in water-ethanol solutions decreased as the proportion of ethanol increased [14]. Increasing the concentration of ethanol in water lowers the boiling temperature and latent heat significantly. The second approach is to ensure that the energy delivered is converted to non-thermal forms after the bubble is formed. The cavitation process itself facilitates this dispersion. Most of the energy driving cavitation is converted into acoustic energy. The shockwaves marking the formation and collapse of the bubble scatter nearly 75% of the absorbed laser energy during pulsed laser-induced cavitation [15]. This enables cavitation to work as a surface cooling mechanism. Comparable results are anticipated for CW-induced cavitation.

CW thermocavitation has been observed to produce bubbles that collapse in a toroidal shape when formed near a solid boundary [16]. When a bubble collapses near a heated solid boundary, the microstream jet will be comprised of colder liquid from outside the heated layer near the boundary. Following the collapse, some of the hot liquid at the boundary will be ejected from the nucleation site outward, where it is removed by a larger-scale external flow. By this process, CW cavitation enables targeted ‘spot-removal’ of heat in the context of a convective cooling system.

To evaluate the effectiveness of optical thermocavitation to enhance heat exchange at microfluidic scales, the temperature field surrounding the bubble must be measured. Direct temperature measurement is prohibited by the magnitude of the acoustic shockwaves typically produced upon bubble formation and collapse. Any sensor fast enough to characterize cavitation dynamics is by necessity small and exposed, making it susceptible to such damage. Further, characterizing a temperature field using point-response sensors is difficult and intrusive. Infrared cameras avoid the hazards associated with cavitation but are costly at the required sampling rates (~1000 Hz). Also, their typical working long infrared wavelengths (~8–15 μm) limit the permissible imaging range inside water due to high absorption.

Laser-induced fluorescence temperature measurement offers a novel option to overcome the challenges of characterizing the cavitation temperature field. Numerous studies utilize Planar Laser-Induced Fluorescence (PLIF) as a technique that takes advantage of property-sensitive fluorescent dye to determine conditions of a medium. For instance, since the first demonstration of laser-induced fluorescence in 1977 by Zare et al. [17] for investigating chemical reactions, PLIF has been adapted as a tool to characterize various aspects of the sciences including particle flow velocity and local concentration of species, among other measurements [18,19].

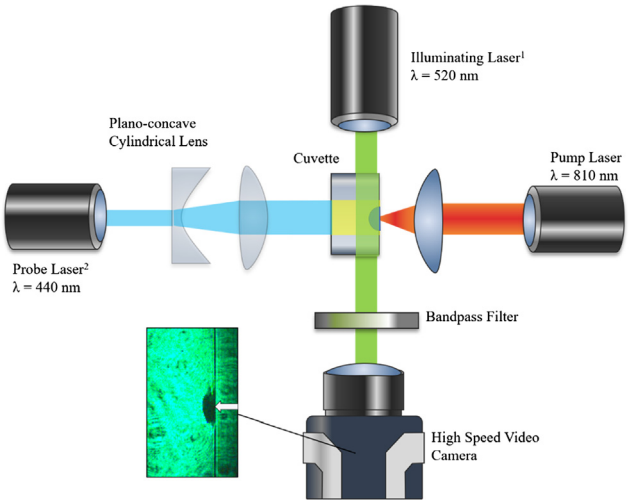

Fig. 1. Experimental setup for shadowgraphy imaging and planar laser-induced fluorescence (PLIF) temperature measurement. Inset shows shadowgraph image of thermal boundary layer on the cuvette wall due to spot heating. The vertical black line on the right side is the cuvette wall, and the laser axis is centered on the white arrow. (1) The illuminating laser is used to illuminate the camera directly for shadowgraphy and is removed during fluorescence measurement. (2) The probe laser excites fluorescence and is inactive for shadowgraphy imaging.

In this work, the capability of temperature-sensitive fluorescing rhodamine-B dye and a high speed digital video camera is explored. Using a laser diode light sheet as the excitation source, PLIF allows inexpensive simultaneous observation of the cavitation bubble and the temperature surrounding it. PLIF is implemented in an optical setup used to produce and characterize cavitation bubbles and an analysis of energy conversion is presented. Shadowgraphy is used as a secondary method to visualize the cavitation events at higher temporal resolution and as qualitative validation of the PLIF temperature field measurements.

2. Experimental setup

A schematic of the experimental setup is depicted in Fig. 1. Cavitation is induced in a solution of aqueous copper nitrate ($Cu(NO_3)_2$), contained in a 1 cm by 1 cm by 4 cm glass cuvette. The cuvette is transparent on all sides in the visible and near-IR spectrum. Cavitation is induced quasi-periodically by a continuous wave (CW) laser diode emitting at 810 nm wavelength with an output of 4.5 W (the *pump* laser), which is focused through a 25.4 mm focal length lens into the cuvette. The beam waist is 0.75 mm in diameter at half-maximum intensity. $Cu(NO_3)_2$ is highly absorptive of near-IR wavelengths, promoting thermocavitation, but is relatively transparent in the violet to yellow visible spectrum, allowing direct video observation of bubble dynamics.

Two imaging methods are employed to observe the temperature field surrounding cavitation bubbles: shadowgraph imaging, which provided high-framerate (10^4 fps) qualitative observation of temperature within the liquid, and planar-laser-induced fluorescence (PLIF) imaging, which gave quantitative temperature measurements at a lower framerate (10^3 fps). A Miro m310 high speed video camera (Vision Research, CA, USA) records perpendicularly to the pump laser axis,

imaging through a Nikon Micro-Nikkor 105 mm f/2.8 lens. The camera uses several zoom lenses to enable a macro field of view of approximately 5 mm by 5 mm for shadowgraphy.

2.1. Shadowgraph imaging

Shadowgraph imaging is included in this study for two reasons. First, it provides a qualitative validation of the PLIF temperature field measurements. Although it does not confirm the measurement of the temperature itself, the liquid heated by the collimated laser experiences a reduction in density and thus a refractive index change, which is manifested within the cuvette and appears as shadows and contours, as seen in inset of Fig. 1. Second, for shadowgraph imaging, rhodamine-B is excluded because its high absorption would prevent laser light from reaching the camera. Thus, shadowgraph imaging uses direct illumination by a 5 mW 520 nm diode laser (Illuminating Laser), which allows video to be recorded at significantly higher framerates (and consequently lower exposure time) than that possible with the much less intense illumination provided by rhodamine-B fluorescence. Shadowgraphy images are recorded at 10,000 fps, whereas PLIF videos are an order of magnitude slower at 1000 fps. Thus, shadowgraph videos can help fill in the gaps, where PLIF may miss some of the short-duration dynamics of cavitation. Fig. 1 shows the experimental arrangement for the shadowgraphy setup and Fig. 2 shows the average time of cavitation events observed.

2.2. PLIF apparatus

PLIF uses stimulated fluorescence to make temperature differences visible. A fluorescent dye (rhodamine-B in this case) is irradiated by an excitation laser beam shaped into a sheet. Under this excitation, dye fluoresces at a different wavelength. Using a video camera and image analysis software, the intensity of fluorescence can be measured. This fluorescence can be correlated with the conditions within the liquid at that location. Rhodamine fluorescence in general, has been found to be sensitive to local temperature, pressure, concentration, or shear. Rhodamine-B ($C_{28}H_{31}ClN_2O_3$) fluoresces primarily with different intensity at different temperatures. Holding everything else approximately constant, then, the fluorescence intensity can be calibrated to provide a non-intrusive measure of the local temperature [20].

A 440 nm, 2 W diode (the *probe*) is shaped into a sheet approximately 1 mm thick by 1 cm wide by a cylindrical plano-concave lens (f = -100 mm) in conjunction with an aspheric lens (f = 100 mm) and continuously transmitted through the side of the cuvette, avoiding reflectance from the meniscus. The rhodamine-B fluoresces within the probe's light sheet, with fluorescence wavelengths typically in the range of 550–570 nm (green-yellow). A longpass filter with cut-off wavelength of 550 nm hides the probe from the camera, and a shortpass filter with a cut-off wavelength of 600 nm blocks the pump from view. Video is recorded at 1000 fps with 990 µs exposure time and 512 × 512 pixels resolution.

The cavitation fluorescence solution consists of 4 mL of $Cu(NO_3)_2$ with rhodamine-B dye added. The concentrations of $Cu(NO_3)_2$ and rhodamine-B by weight are 0.48 g $Cu(NO_3)_2$ and 0.07 mg rhodamine-B to 1 g of deionized water. The boiling point of this solution was measured at 93 °C.

Raw images are digitally rotated and cropped using ImageJ software to remove the cuvette wall and areas outside of the probe laser. The cropped image shows an area of approximately 3.5 W mm × 9 H mm centered on the pump axis (Fig. 3).

To calibrate the fluorescence setup, the cuvette is filled with rhodamine-B solution and heated to thirteen different temperatures up to 85 °C. Beyond 85 °C, evaporation becomes quite rapid, altering the solution concentration and invalidating any measurement. A thermocouple is used to verify the temperature of the liquid within the cuvette to ± 0.5 °C. Two hundred frames of video are recorded at each temperature. Using a Python image analysis script, each video frame is divided into a 40 × 40 grid to provide 1600 cells. The intensity of the fluorescence is measured (as the average RGB value) within each cell of the grid and averaged over all 200 frames to establish a reference value for that temperature. Following this procedure ensures that every region of the image is calibrated uniquely against an individual cell covering approximately 0.09 mm × 0.2 mm. Individual cell calibration enables that the extinction of the excitation laser sheet is accounted for in the calibration process. Thirteen temperatures are used to establish an intensity-temperature curve. Eq. (1) is used to solve for the slope of each grid square's calibration curve.

$$m_g = \frac{I - I_{ref}}{T - T_{ref}} \tag{1}$$

The slope, m_g, is averaged for each sequential pair of temperatures, $T - T_{ref}$ and the corresponding measured intensity change, $I - I_{ref}$. Fig. 4 shows the calibrated intensity curve for the 4 sample vertical regions of Fig. 3. Each region has a different calibration curve due to the attenuation of the probe laser as it travels throughout the medium.

Rhodamine-B is reported in literature to vary approximately linearly with temperature. Sakakibara used a second-order least-squares fit and found near-linear temperature vs intensity, of approximately 1 °C per 2% decrease in intensity up to 70 °C [21]. Chen and Chauhan also found good agreements with a linear fit under 90 °C [22,23].

As seen in Fig. 4, the intensity curves for each grid square are closely approximated by a linear fit. The R^2 values remained consistently above 0.9 for all cells. The linear relationship agrees with findings in other applications of PLIF that used rhodamine-B. The exact slope of the fit depends on the concentration of rhodamine-B, excitation power, and the optical setup. To prevent error due to slight variations in the optical setup among experiments, the calibration process is repeated after each experiment without touching the setup except to activate the hot plate. The calibration reveals a slightly diminished temperature sensitivity compared to the findings of Sakakibara and Chen [21,22], with an average of 10 °C change in temperature corresponding to a 3% change in intensity. Between three calibration trials, the maximum observed variation in intensity at a given temperature was ± 5%, corresponding to ± 17 °C uncertainty in temperature. The maximum variation in

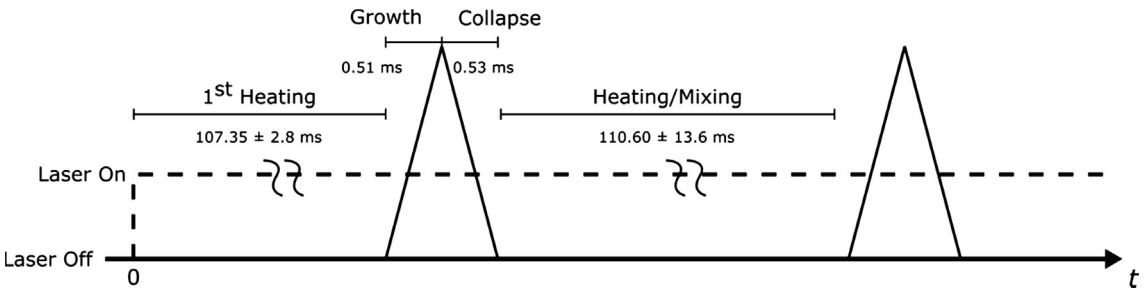

Fig. 2. Average thermocavitation event durations for the experiments presented. The first bubble is excluded from averages due to larger random heating variation. The standard deviation of the growth and collapse is ± 0.02 ms.

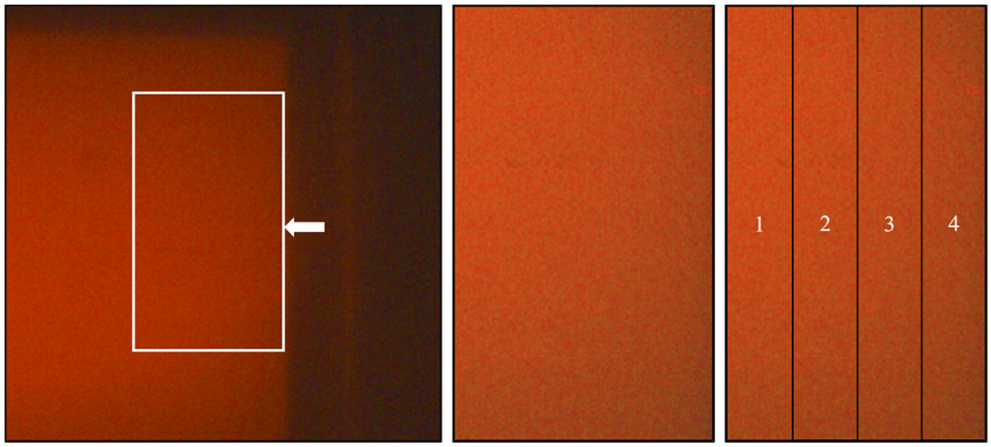

Fig. 3. Raw experiment image (left) with arrow indicating pump laser axis and rectangular box indicating the cropped region (middle). Gridded image (right) demonstrates four vertical regions used for example temperature calibration in Fig. 4.

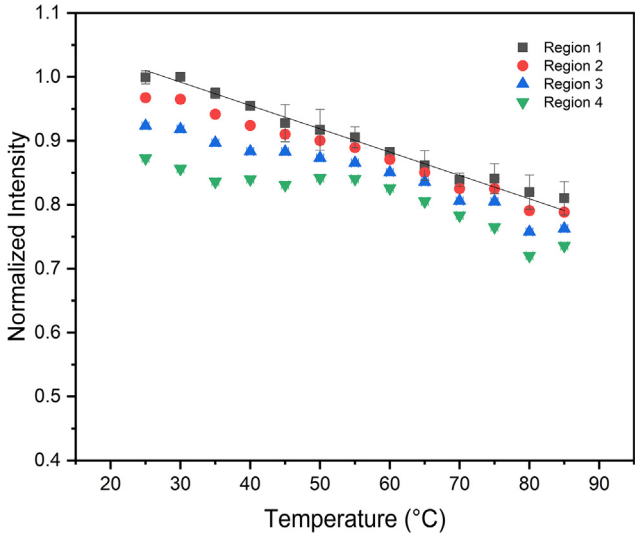

Fig. 4. Fluorescent intensity versus temperature for typical grid cells. The points indicate the normalized RGB value within that cell. A linear fit is developed for each grid location. Each symbol corresponds to the four vertical regions of Fig. 3. Y-error bars, defined by standard error of 3 experiments, are shown for Region 1.

intensity was observed at 80 °C, at the top of the calibration range. At lower temperatures, the variation in intensity is generally reduced. Over the entire calibration range, the average variation in intensity was ± 2%, corresponding to a ± 7 °C uncertainty in temperature.

The temperature was calculated using Eq. (2), which is found by rearranging Eq. (1).

$$T = \frac{I - I_{ref}}{m_g} + T_{ref} \tag{2}$$

It is worth noting that the concentration of rhodamine-B in this study is far greater than typical PLIF applications use (typically on the order of 0.0001 mg rhodamine-B/g water). High video framerates necessitate short frame exposure times, minimizing the amount of light that can reach the camera sensor during each frame. Increased concentration of rhodamine-B results in brighter fluorescence. However, there is a red-shift in the fluorescence, as the rhodamine-B partially reabsorbs and re-emits its own light [24]. As such, the fluorescence is not at rhodamine-B's nominal 550 nm emission peak, but rather between 570 and 600 nm. A bandpass filter of 560 ± 10 nm blocks all fluorescence from the camera's view, indicating that fluorescence is occurring outside that range.

Another consequence of the elevated rhodamine-B concentration is the selection of excitation lasers. Rhodamine-B has an absorption peak at approximately 540 nm; typically green-wavelength lasers are used to stimulate fluorescence. The increased concentration permits a 520 nm beam to penetrate only approximately a millimeter into the liquid. Thus, the 440 nm probe laser is selected for its balance of transmission and absorption as it can pass through the entire cuvette exciting the rhodamine-B.

Two mechanisms that may affect the temperature measurements are the luminescence [25], referring to the flash of emitted light, and the shockwaves produced upon bubble collapse. Regarding the former, Ohl and Lauterborn found that luminescence from pulsed laser-induced bubbles requires highly spherical bubbles, with more aspherical bubbles emitting light with weaker intensity [26]. The naturally hemispherical nature of thermocavitation suggests by this reasoning that little or no light emission occurs; none has been reported in literature for thermocavitation. Regarding the latter, the emitted shockwave propagates at a minimum of the speed of sound and is consequently a much shorter time duration (ns) than the video frame (1 ms). The luminescence typically also lasts a few nanoseconds for pulsed laser-induced bubbles [27]. Thus, the most valid reasons why potential effects of luminescence on the temperature measured around the bubbles are neglected are because luminescence is likely inexistent for hemispherical bubbles produced by thermocavitation, and its heat diffusion time (~1.7 s) given the length scale to propagate from the center to the edge of the bubble is so long compared with the time scale of the bubbles that its effect is virtually undetectable.

3. Results

3.1. Shadowgraph temperature field

3.1.1. Heating

Fig. 5 depicts the heating phase between laser activation and bubble formation, which lasted approximately 120 ms. The thermal boundary layer is seen as a dark region appearing on the cuvette wall and gradually growing wider and spreading upwards as the liquid heats and becomes less dense.

3.1.2. Bubble

The results of the collapse of the bubble can be observed as relative temperature differences denoted by contours in the image. A series of still frames showing this process is depicted in Fig. 6. The bubble first appears in the initial frame; it appears to last approximately 600 μs before collapsing. A short delay later, at approximately 900 μs after nucleation, a rebound bubble appears and vanishes before the next time

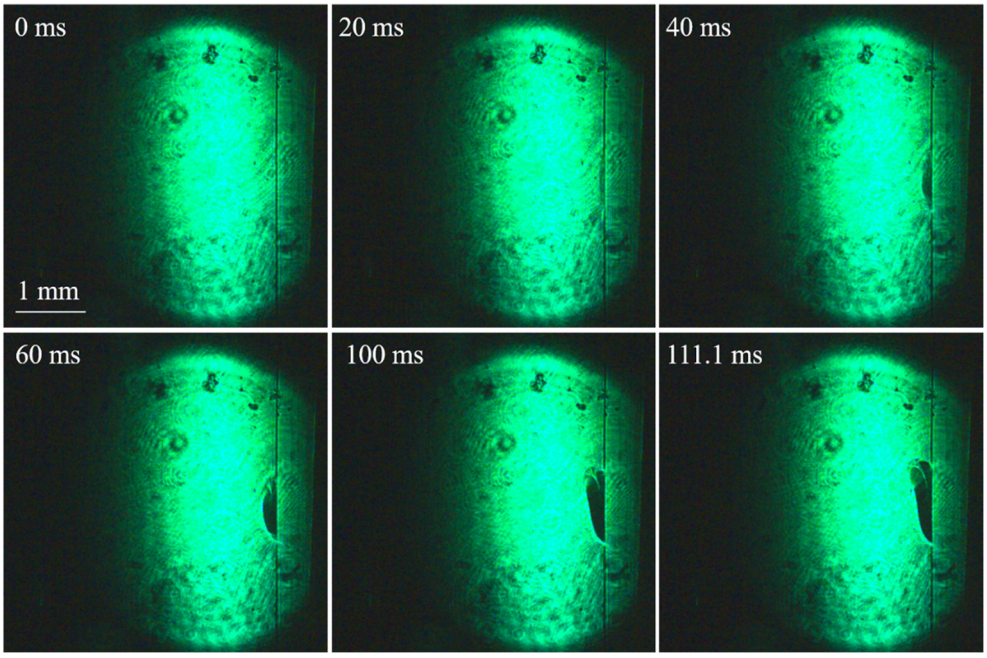

Fig. 5. Shadowgraph images showing the growth of the thermal boundary layer prior to bubble formation. The labels indicate the length of time after the laser is activated.

step (100 μs) due to its short lifetime relative to the recording framerate.

3.1.3. Mixing

After the bubble collapses, a stream of heated liquid is seen to migrate away from the nucleation site. Fig. 7 shows this ejection, accompanied by a view of the significantly thinned thermal boundary layer. Due to the high framerate of the shadowgraph videos, the full regrowth of the thermal boundary layer until the occurrence of the second cavitation event was not obtained, but over 16 bubbles with the same experiment parameters, the average delay between bubbles was 110.6 ± 13.6 ms (Fig. 2).

3.2. Fluorescence temperature measurement

In accordance with the shadowgraphy images, temperature measurements were grouped chronologically into three phases: the heating phase (Fig. 8), bubble phase (Fig. 9), and mixing phase (Fig. 10). The heating phase is defined as the time between the pump laser activation and bubble nucleation. The bubble phase lasts from the time the bubble appears until no bubble is visible for two consecutive video frames. In many cases, a cavitation bubble is observed to rebound from its initial collapse; for purposes of this study, the bubble phase is defined as including these subsequent bubble oscillations. The mixing phase starts after the last bubble collapses and no motion is observed.

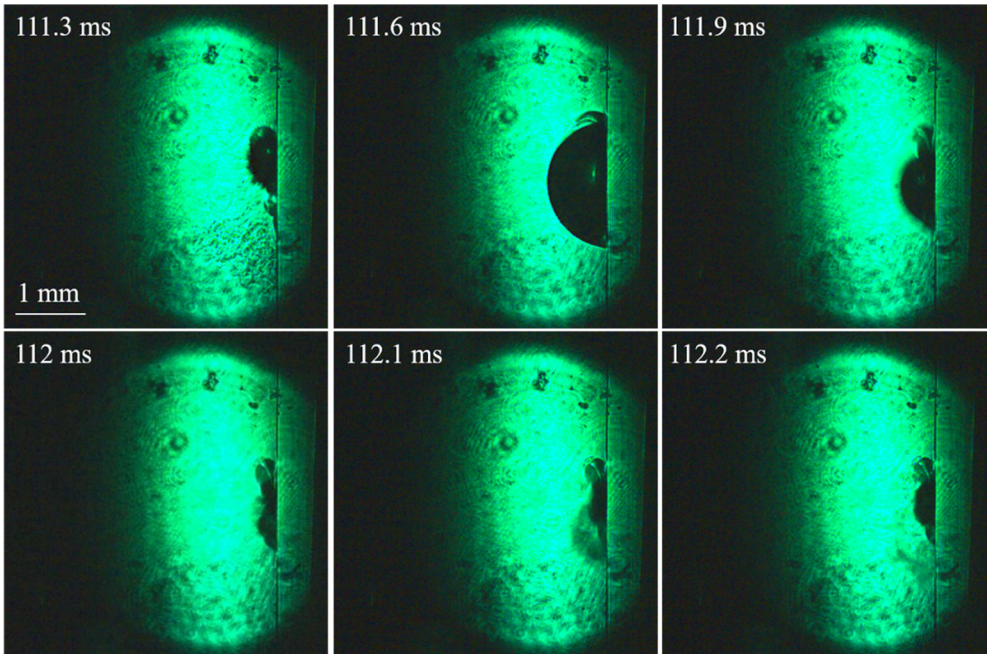

Fig. 6. Shadowgraph images showing the bubble growth and collapse. The labels indicate the length of time after the bubble nucleation.

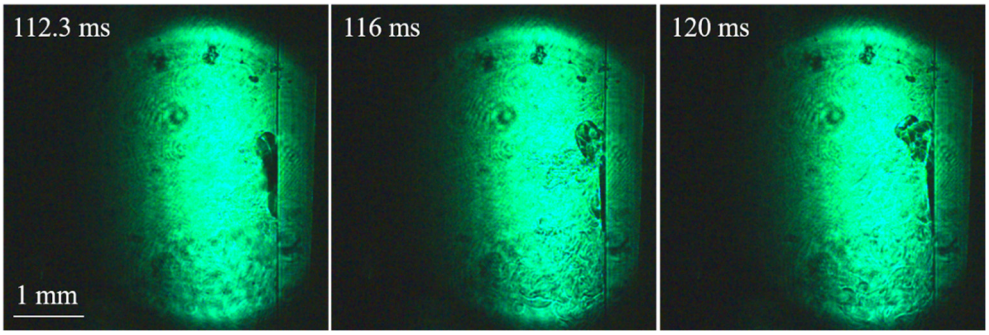

Fig. 7. Shadowgraph images showing the ejection of hot liquid after cavitation bubble collapse. The labels indicate the length of time after the bubble nucleation.

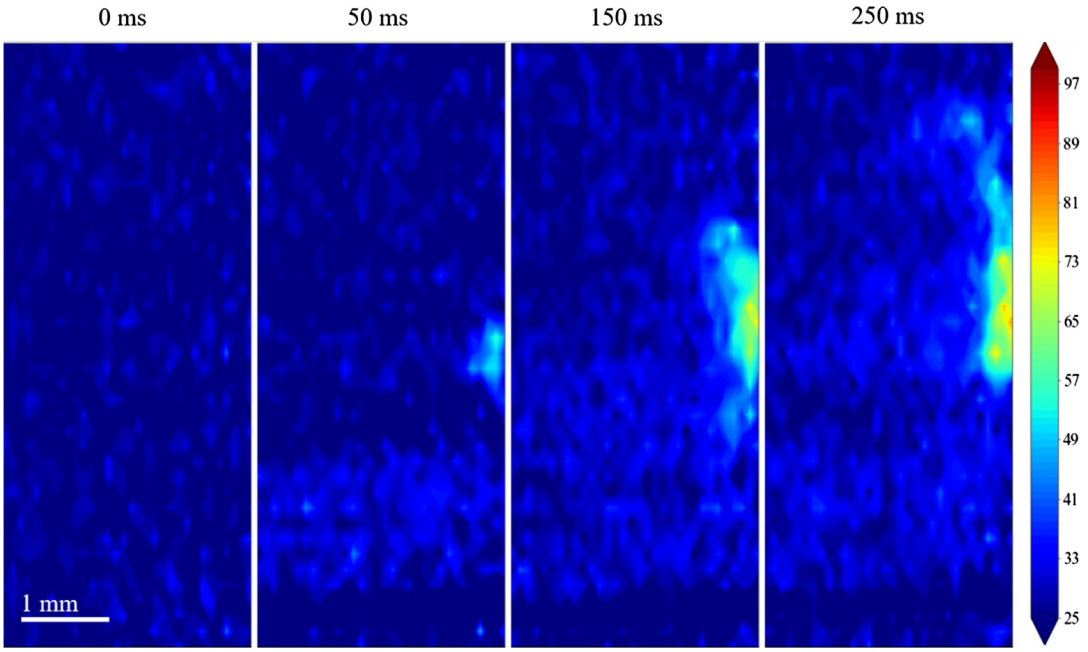

Fig. 8. Temperature measurements during the heating phase, prior to bubble nucleation. The time listed above each image represent the amount of time that has passed since the activation of the pump laser. The scale on the right is temperature in ˚C.

The temperature-fluorescence relationship is calibrated up to 85 ˚C, and linearly extrapolated beyond that limit. Cavitation will be seen to occur above that limit, so there is the potential for deviation from the calibrated line.

3.2.1. Heating

The heating phase for the temperature measurement study lasted approximately 262 ms, from the instant the laser was activated until the first bubble nucleated. Fig. 8 shows selected frames from this period. During this time, the highest observed temperature was 98 ˚C. The thermal boundary layer is observed to start at the point of irradiation and spread vertically upwards, driven by natural convection for 260 ms after the laser is activated.

3.2.2. Bubble

The heated liquid is driven outward by the growing bubble (Fig. 9), expanding the heated volume. The bubble itself appears as anomalous region – while it is undoubtedly quite hot, the temperature reported within the bubble is due to the absence of fluorescing substance, appearing very dark on video. Further, the area around the bubble seems to have abruptly decreased in temperature – there is less ‘noise’, defined as small temperature fluctuations that appear as slightly lighter patches on the image during the bubble growth than immediately before or after. Rhodamine-B is negligibly pressure-sensitive [28], however, the sudden cumulative changes in pressure, shear and concentration during the event of the bubble is likely influencing the calculated temperature. Further, the long exposure time used to capture fluorescent intensity exceeds the lifetime of the bubble, causing a blurred boundary. As such, the temperature measurements within the bubble, immediately after its nucleation and all the way until its collapse, are neglected to ensure that any effects of varying medium properties or Rhodamine B concentration gradients are ignored. The frame with the bubble present is included in Fig. 9 as a reference for maximum size, with the bubble periphery outlined in white. Shortly after the bubble collapses (264 ms), however, the thermal boundary layer appears nearly absent. A relatively small volume of warm liquid is seen ejected from the bubble site. The maximum temperature just prior to the bubble at 262 ms is 98 ˚C, and then within 5 ms (at 267 ms) the maximum temperature drops to 57.7 ˚C. Correspondingly, the average temperature within the field of view at 262 ms is 29 ˚C, which cools to 27 ˚C by 267 ms. Thus, a strong cooling effect is observed in the neighborhood of the bubble.

3.2.3. Mixing

The mixing phase extended from the collapse of the bubble for the next 292 ms, ending upon the formation of a new bubble. Thus, the mixing phase after one bubble is also the heating phase for the next. There is some difference in the length of heating phases between

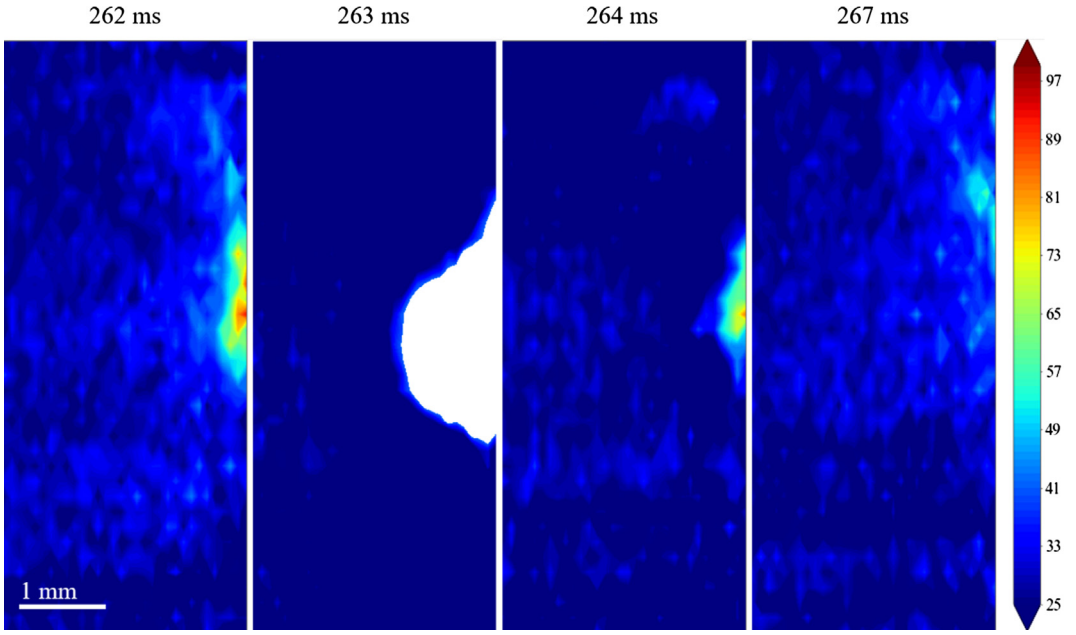

Fig. 9. Temperature measurements during the bubble's growth, near its maximum diameter, and during its collapse. The time listed above each image represent the amount of time that has passed since the activation of the pump laser. The scale on the right is temperature in °C.

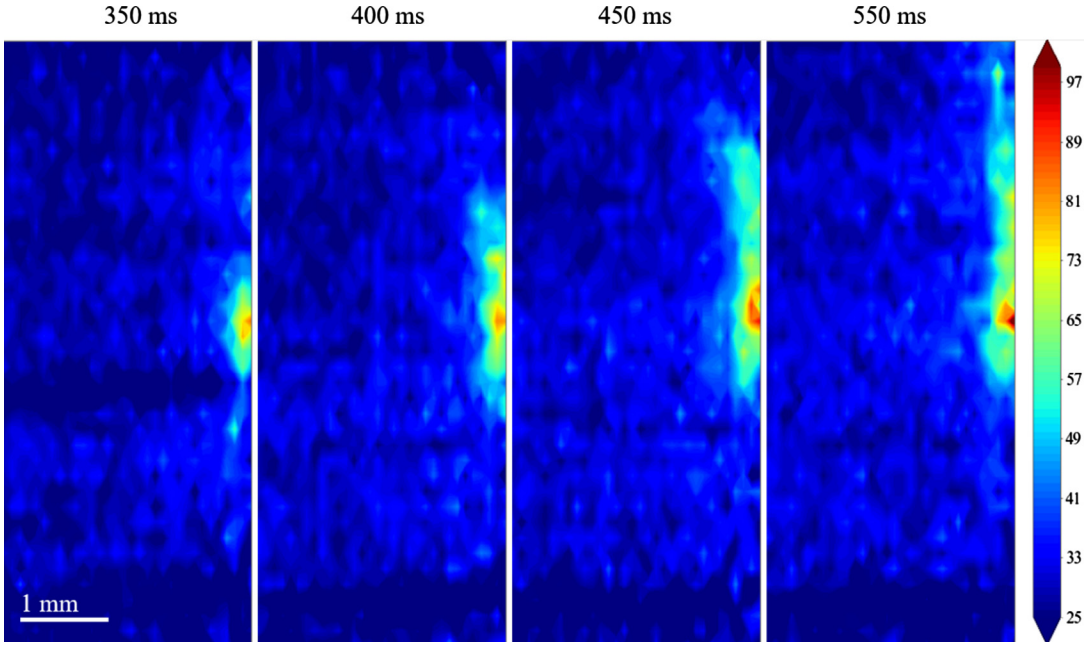

Fig. 10. Temperature measurements during the mixing phase, after the collapse of the bubble. The time listed above each image represent the amount of time that has passed since the activation of the pump laser. The scale on the right is temperature in °C.

bubbles – this jitter is likely due to the stochastic nature of thermo-cavitation, the inherent variations of temperature around the focal point, and the relatively long focal length lens used in the experimental setup; Padilla-Martinez et al, observed that increasing the energy density makes optical cavitation occur more consistently [3]. However, under continuous irradiation, the energy added to the liquid must be dispersed – otherwise, the frequency should increase as the liquid heats up. The collapse of the cavitation bubble appears to cool the liquid significantly, offsetting the heat added by the laser. The apparent cooling effect is noticed by comparing the temperatures of 262 ms and 264 ms, 1 ms after the collapse of the bubble. As the bubble collapses, the previously fluorescing dye-absent-bubble is quickly refilled, possibly affecting observed temperatures due to an increase in rhodamine-B concentration. However, an increase in concentration would have a negative effect appearing as an increase in temperature. The opposite is seen in the PLIF sequence of the mixing phase suggesting that the liquid is reheating. The mixing phase, as depicted in Fig. 10 shows the dispersion and regrowth of the thermal boundary layer culminating at the formation of the subsequent bubble. This temperature increase is attributed to the thermal boundary layer resurfacing as imaged in the shadowgraph sequence of Fig. 5.

4. Discussion

The peak temperature, 98 °C, prior to cavitation is seen to exceed the boiling point of the solution (measured at approximately 93 °C) –

correlating well with Padilla-Martinez et al assertion that thermocavitation is driven by a measure of superheat. However, possibly due to limitations in calibration and physical limitations of rhodamine-B fluorescence at elevated temperatures, the large degree of superheat anticipated by Padilla-Martinez et al, is not seen. Further, the temperature-fluorescence calibration is extrapolated past 85 °C; it is likely that deviation from the linear approximation will occur at superheated temperatures.

After the bubble occurs, the heat that drove bubble formation is effectively dispersed. The maximum temperature diminishes considerably from 98 to 57.7 °C, and the distribution of heated liquid is severely diminished in the observed plane. Fig. 9 shows the bubble growing to a diameter of several times greater than the thickness of the thermal boundary layer observed and, upon collapse, pushing much of the surrounding hot liquid away from the nucleation point.

The large decrease in temperature suggests the bubble drives an energy conversion, from thermal to some other form. The likely candidate explaining this dispersion is the acoustic shockwaves emitted upon bubble formation and collapse. An energy balance is developed to compare the remaining heat and the dispersed acoustic energy, relative to the laser energy absorbed by the liquid.

A scale argument can be developed to estimate the conversion of optical energy into heat and subsequently split between acoustic emission and remnant heat. Assuming all the optical energy is absorbed and converted to heat, and neglecting work done by the expansion and contraction of the bubble, the net change in heat from before the laser until the bubble forms is equal to the sum of the remnant heat and the released acoustic energy.

$$E_{added} = E_{rem} + E_{acoustic} \tag{3}$$

The thermal energy added by the laser can be approximated simply by $\rho V c \Delta T_i$, where ρ is the density, V the volume, c the specific heat, and ΔT_i the change in temperature, which is the measured temperature just prior to the bubble minus the initial liquid temperature; the remnant energy can be calculated using the same expression, changing the subscript.

$$\rho V c \Delta T_i = \rho V c \Delta T_r + E_{acoustic} \tag{4}$$

Simplifying for $E_{acoustic}$, where T_{meas} indicates measured temperature, subscript i describes the pre-bubble state – that is, the frame just prior to the appearance of the bubble, subscript o represents the post-bubble state – the first frame after the collapse of the bubbles, and ∞ the bulk temperature:

$$E_{acoustic} = \rho V c (\Delta T_i - \Delta T_r) \tag{5a}$$

$$E_{acoustic} = \rho V c ((T_{meas,i} - T_\infty) - (T_{meas,o} - T_\infty)) \tag{5b}$$

$$E_{acoustic} = \rho V c (T_{meas,i} - T_{meas,o}) \tag{5c}$$

A further assumption – heat does not diffuse beyond the field of view of the frame. In Figs. 8–10 the region of heated liquid only once seems to approach the edge of the frame. With this assumption, however, within the plane of fluorescence, the temperature differences are readily calculated within each grid square. The sum of the temperature changes pre- and post-bubble in all grid squares, n, then determines the acoustic energy release. The result is relatively insensitive to the actual measured volume, if the entire heated region is within the frame. Unheated regions will have a minimal difference in temperature and thus will zero themselves out of the calculation.

$$E_{acoustic} = \rho V c \sum_n (T_{meas,i} - T_{meas,o}) \tag{6}$$

Normalizing Eq. (6) by the total energy prior to bubble formation produces an expression for the percentage of energy converted from thermal to acoustic.

$$\frac{E_{acoustic}}{\rho V c \sum_n (T_{meas,i} - T_{meas,\infty})} = \frac{\rho V c \sum_n (T_{meas,i} - T_{meas,o})}{\rho V c \sum_n (T_{meas,i} - T_{meas,\infty})} \tag{7}$$

And, by simplifying:

$$\frac{E_{acoustic}}{\rho V c \sum_n (T_{meas,i} - T_{meas,\infty})} = \frac{\sum_n (T_{meas,i} - T_{meas,o})}{\sum_n (T_{meas,i} - T_{meas,\infty})} \tag{8}$$

To account for noise, the mean of the sum of temperatures for 10 ms prior to the bubble and ten after the bubble were used in computing the energy changes. For the four bubbles observed on video – depicted in Figs. 9, S1, S2, and S3, approximately 47%, 34%, 2%, and 46% of the energy is released after the bubble collapses based on this analysis. It is immediately apparent that the size of the bubble plays a large role in the energy conversion – bubbles in Figs. S1 and S2 are significantly smaller than Figs. 9 and S3 and have significantly smaller energy dispersion. The analysis was repeated for a second dataset, containing 8 bubbles produced using the same setup. The energy dispersion ranged from 0% – resulting from several very small bubbles – to 46% with larger ones. Future study will work to explore the relationship between bubble dynamics and heat dissipation.

5. Conclusion

The temperature field as it develops during optical thermocavitation has been studied. As demonstrated by the shadowgraphy and PLIF measurements, the thermal boundary layer arising from the laser-spot heating near the cuvette wall grows until a bubble nucleates. Because of the rapid heating and relatively small heated volume, explosive vaporization occurs. The growth and collapse of the bubble then disperses the heated liquid. The thermal boundary layer was seen to disappear and regrow from near-ambient temperature. Liquid farther away from the irradiation point undergoes little to no heating. A marked decrease in sensible heat in the neighborhood of the bubble is observed. This is the first experimental observation of the temperature field surrounding cavitation bubbles induced by continuous-wave lasers. Future work includes measuring the energy dispersed acoustically, using a hydrophone for example, rather than estimating based on residual temperatures.

This cooling effect facilitates cavitation as a targeted, non-intrusive, spot agitator to provide increased convective cooling to desired areas within microfluidic devices. The bubbles are believed to disperse the thermal energy used to form them by both advective mixing and conversion to acoustic energy. This dispersion allows cavitation to enhance a localized cooling process, despite adding heat to the liquid overall. Future work includes examining the dynamics of the thermal boundary layer in a liquid that is externally heated in addition to the laser's spot heating, and exploration of the growth of the thermal boundary layer over an extended period and through the occurrence of multiple sequential bubbles. The overall goal of plif is to characterize the 3-d temperature field surrounding cavitation bubbles by shifting the excitation light sheet, and to combine it with an optical shockwave characterization technique to provide real-time measurement of bubble dynamics, temperature, and pressure. The factors governing bubble formation, namely, irradiation energy density, absorptivity, solution specific heat, and surface tension, remain to be studied to determine their effects on the thermal-to-acoustic energy conversion resulting from the bubble dynamics.

Acknowledgements

The authors would like to thank Cynthia Ajawara, Seyed Mahdi Akbarimoosavi, Ismael Martinez, and Ruddy Calderon for their laboratory assistance. Discussions with Dr. Juan-Pablo Padilla Martinez, Dr. Monica Martinez, Dr. Marko Princevac, and Dr. Lorenzo Mangolini have been invaluable in advancing this work.

Funding

This work was supported by the National Science Foundation [NSF-CBET grant 1403508], the CONACyT [grant CB-2015-01-254304], and the UCMEXUS Dissertation Research Grant. Participation of V. Robles was further enabled by the Ford Foundation Predoctoral Fellowship.

Competing financial interests

The authors declare no competing financial interests.

Appendix A. Supplementary material

Supplementary data to this article can be found online at https://doi.org/10.1016/j.expthermflusci.2019.01.030.

References

[1] E.F. Carome, N.A. Clark, C.E. Moeller, Generation of acoustic signals in liquids by ruby laser-induced thermal stress transients, Appl. Phys. Lett. 4 (1964) 95–97, https://doi.org/10.1063/1.1753985.
[2] L.F. Devia-cruz, F.G. Perez-Gutierrez, D. Garcia-Casillas, G. Aguilar, S. Camacho-Lopez, D. Banks, High resolution optical experimental technique for computing pulsed laser-induced cavitation bubble dynamics in a single shot, Atomiz. Sprays 23 (2013) 475–485, https://doi.org/10.1615/AtomizSpr. 2013007139.
[3] J.P. Padilla-Martinez, C. Berrospe-Rodriguez, G. Aguilar, J.C. Ramirez-San-Juan, R. Ramos-Garcia, Optic cavitation with CW lasers: a review, Phys. Fluids. 26 (2014), https://doi.org/10.1063/1.4904718.
[4] P. Prentice, A. Cuschieri, K. Dholakia, M. Prausnitz, P. Campbell, Membrane disruption by optically controlled microbubble cavitation, Nat. Phys. 1 (2005) 107–110, https://doi.org/10.1038/nphys148.
[5] R. Dijkink, C.-D. Ohl, Laser-induced cavitation based micropump, Lab Chip. 8 (2008) 1676, https://doi.org/10.1039/b806912c.
[6] Stanislav F. Rastopov, Anatoly T. Sukhodolsky, Sound generation by thermo-cavitation-induced cw laser in solutions, Optical Radiation Interaction with Matter, vol. 1440, International Society for Optics and Photonics, 1991, pp. 127–135.
[7] X. Huang, P.A. Quinto-Su, S.R. Gonzalez-Avila, T. Wu, C.D. Ohl, Controlled manipulation and in situ mechanical measurement of single co nanowire with a laser-induced cavitation bubble, Nano Lett. 10 (2010) 3846–3851, https://doi.org/10.1021/nl101051t.
[8] J.G. Fujimoto, W.Z. Lin, E.P. Ippen, C.A. Puliafito, R.F. Steiner, Time-resolved studies of Nd:YAG laser-induced breakdown, Investig. Ophthalmol. Vis. Sci. 26 (1985) 1771–1777.
[9] O. Yavas, P. Leiderer, H.K. Park, C.P. Grigoropoulos, C.C. Poon, W.P. Leung, N. Do, A.C. Tam, Optical reflectance and scattering studies of nucleation and growth of bubbles at a liquid-solid interface induced by pulsed laser heating, Phys. Rev. Lett. 70 (1993) 1830–1833, https://doi.org/10.1103/PhysRevLett. 70.1830.
[10] J.C. Ramirez-san-juan, E. Rodriguez-Aboytes, A.E. Martinez-Canton, O. Baldovino-Pantaleon, A. Robledo-Martinez, N. Korneev, R. Ramos-garcia, Time-resolved analysis of cavitation induced by CW lasers in absorbing liquids, Opt. Express. 18 (2010) 8735–8742, https://doi.org/10.1364/OE.18.008735.
[11] P.A. Quinto-Su, M. Suzuki, C.-D. Ohl, Fast temperature measurement following single laser-induced cavitation inside a microfluidic gap, Sci. Rep. 4 (2014) 1–6, https://doi.org/10.1038/srep05445.
[12] C.Y. Lee, C.L. Chang, Y.N. Wang, L.M. Fu, Microfluidic mixing: a review, Int. J. Mol. Sci. 12 (2011) 3263–3287, https://doi.org/10.3390/ijms12053263.
[13] R.H. Liu, J. Yang, M.Z. Pindera, M. Athavale, P. Grodzinski, Bubble-induced acoustic micromixing, Lab Chip. 2 (2002) 151, https://doi.org/10.1039/b201952c.
[14] S.F. Rastopov, A.T. Sukhodol'sky, Cluster nucleation in the process of CW laser induced thermocavitation, Phys. Lett. A 149 (1990) 229–232, https://doi.org/10.1016/0375-9601(90)90334-K.
[15] A. Vogel, W. Lauterborn, Acoustic transient generation by laser-produced cavitation bubbles near solid boundaries, J. Acoust. Soc. Am. 84 (1988) 719–731, https://doi.org/10.1121/1.396852.
[16] J.P. Padilla-Martinez, J.C. Ramirez-San-Juan, N. Korneev, D. Banks, G. Aguilar, R. Ramos-Garcia, Breaking the Rayleigh-Plateu instability limit using thermo-cavitaion within a droplet, Atomiz. Sprays 23 (2013) 487–503, https://doi.org/10.1615/AtomizSpr. 2013007155.
[17] A. Schultz, H.W. Cruse, R.N. Zare, Laser-induced fluorescence: a method to measure the internal state distribution of reaction products, J. Chem. Phys. 57 (1972) 1354–1355, https://doi.org/10.1063/1.1678401.
[18] A. Cessou, U. Meier, D. Stepowski, Applications of planar laser induced fluorescence in turbulent reacting, Meas. Sci. Technol. 11 (2000) 887–901.
[19] A. Charogiannis, J.S. An, C.N. Markides, A simultaneous planar laser-induced fluorescence, particle image velocimetry and particle tracking velocimetry technique for the investigation of thin liquid-film flows, Exp. Therm. Fluid Sci. 68 (2015) 516–536, https://doi.org/10.1016/j.expthermflusci.2015.06.008.
[20] J.P. Crimaldi, Planar laser induced fluorescence in aqueous flows, Exp. Fluids 44 (2008) 851–863, https://doi.org/10.1007/s00348-008-0496-2.
[21] J. Sakakibara, K. Hishida, M. Maeda, Measurements of thermally stratified pipe flow using image-processing techniques, Exp. Fluids 16 (1993) 82–96, https://doi.org/10.1007/BF00944910.
[22] Y.Y. Chen, A.W. Wood, Application of a temperature-dependent fluorescent dye (Rhodamine B) to the measurement of radiofrequency radiation-induced temperature changes in biological samples, Bioelectromagnetics 30 (2009) 583–590.
[23] V.M. Chauhan, R.H. Hopper, S.Z. Ali, E.M. King, F. Udrea, C.H. Oxley, J.W. Aylott, Thermo-optical characterization of fluorescent rhodamine B based temperature-sensitive nanosensors using a CMOS MEMS, Sens. Actuators B. Chem. 192 (2014) 126–133, https://doi.org/10.1016/j.snb.2013.10.042.
[24] C.V. Bindhu, S.S. Harilal, Effect of the excitation source on the quantum-yield measurements of rhodamine B laser dye studied using thermal-lens technique, Anal. Sci. 17 (2001) 141–144, https://doi.org/10.2116/analsci.17.141.
[25] D.J. Flannigan, K.S. Suslick, Plasma formation and temperature measurement during single-bubble cavitation, Lett. Nat. 434 (2005) 52–55, https://doi.org/10.1038/nature03400.1.
[26] C.D. Ohl, O. Lindau, W. Lauterborn, Luminescence from spherically and aspherically collapsing laser induced bubbles, Phys. Rev. Lett. 80 (1998) 393–396.
[27] O. Baghdassarian, B. Tabbert, G.A. Williams, Luminescence characteristics of laser-induced bubbles in water, Phys. Rev. Lett. 83 (1999) 2437–2440.
[28] J.J. Shah, M. Gaitan, J. Geist, Generalized temperature measurement equations for rhodamine B dye solution and its application to microfluidics, Analyt. Chem. 81 (2009) 8260–8263.